Geochemistry, Geophysics, Geosystems®

AGU ADVANCING EARTH AND SPACE SCIENCES

RESEARCH ARTICLE
10.1029/2024GC011732

Microseismicity Around Loki's Castle Hydrothermal Vent Field Reveals the Early Stages of Detachment Faulting at the Mohns-Knipovich Ridge Intersection

Matthias Pilot[1,2], Marie Jakobsen Lien[3], Vera Schlindwein[1,2], Lars Ottemöller[3], and Thibaut Barreyre[3,4,5]

[1]Helmholtz Centre for Polar and Marine Research, Alfred Wegener Institute, Bremerhaven, Germany, [2]Faculty of Geosciences, University of Bremen, Bremen, Germany, [3]Department of Earth Science, University of Bergen, Bergen, Norway, [4]Department of Earth Science, Centre for Deep Sea Research, University of Bergen, Bergen, Norway, [5]Now at CNRS, University of Western Brittany (UBO), Plouzané, France

Abstract At slow to ultraslow spreading ridges, the limited melt supply results in tectonic accretion and the exhumation of mantle rocks. Melt supply is focused toward volcanic centers where magmatic accretion dominates. In areas where the ridges reorientate, both types of accretion can occur across the ridge axis with detachment faults developing on the inside corners and hydrothermal vent fields located in close proximity. Microseismicity studies improve the understanding of the tectonic processes at detachment faults and their interplay with hydrothermal vent systems, but are mostly limited to mature detachment faults or short deployment times. This study presents results from a ∼11 months ocean bottom seismometer deployment around the Loki's Castle hydrothermal vent field at the intersection of the slow to ultraslow spreading Mohns and Knipovich Ridge. We observe seismicity to be highly asymmetric with the majority of the plate divergence being accommodated by an emerging detachment fault at the inside corner of the intersection west of Loki's Castle. Seismic activity related to the detachment fault displays a distinct contrast, with continuous low-magnitude events occurring at depth and episodic large-magnitude events concentrated in clusters within the footwall. The detachment fault shows no significant roll-over at shallow depths and the locus of spreading is located east of the detachment. These results suggest that the detachment fault west of Loki's Castle is at an early development stage.

Plain Language Summary At mid-ocean ridges, Earth's tectonic plates spread apart and the created space is filled by rising magma. In areas where spreading is slowest, there is not enough magma available to create new oceanic crust and existing oceanic crust is being pulled upwards during spreading. This results in earthquakes along cracks known as detachment faults. Often close by to these faults, hot mineral-rich water comes out through chimneys at the seafloor, known as hydrothermal vents. Seismometers placed along the seafloor can record small earthquakes related to spreading processes. Scientists have used these earthquakes to study such processes, but they mostly focus on long-lived detachment faults or study them for short periods. This study looks at nearly a year of data from seismometers placed around the Loki's Castle hydrothermal vent field, located where two slow-spreading ridges meet in the Norwegian-Greenland Sea. The findings show that most of the tectonic activity is related to a detachment fault in its early stages west of Loki's Castle. The fault is continuously active with small earthquakes at depth, but occasional large earthquakes occur focused in areas below the fault's surface.

Key Points:

- Most of the plate divergence at the Mohns-Knipovich intersection is accommodated by an emerging detachment fault west of Loki's Castle
- The largest magnitude events occur episodically within the footwall of the detachment, including indications for antithetic normal faults
- Loki's Castle is located apart from the detachment fault where the brittle-ductile-transition shallows along the axial volcanic ridge

Supporting Information:

Supporting Information may be found in the online version of this article.

Correspondence to:

M. Pilot,
matthias.pilot@awi.de

Citation:

Pilot, M., Lien, M. J., Schlindwein, V., Ottemöller, L., & Barreyre, T. (2024). Microseismicity around Loki's Castle hydrothermal vent field reveals the early stages of detachment faulting at the Mohns-Knipovich Ridge intersection. *Geochemistry, Geophysics, Geosystems*, *25*, e2024GC011732. https://doi.org/10.1029/2024GC011732

Received 27 JUN 2024
Accepted 8 NOV 2024

Author Contributions:

Conceptualization: Vera Schlindwein, Thibaut Barreyre
Data curation: Vera Schlindwein
Formal analysis: Matthias Pilot, Marie Jakobsen Lien, Vera Schlindwein
Funding acquisition: Thibaut Barreyre
Investigation: Matthias Pilot
Methodology: Matthias Pilot, Vera Schlindwein, Lars Ottemöller
Supervision: Vera Schlindwein, Lars Ottemöller
Visualization: Matthias Pilot

1. Introduction

At slow and ultraslow spreading ridges, the melt supply is limited and available melt is focused toward volcanic centers along undulations of lithospheric thickness (J. Chen, Olive, & Cannat, 2023; Magde & Sparks, 1997; Meier et al., 2021; Standish et al., 2008). Around volcanic centers, most of the plate divergence is accommodated by magmatic accretion, resulting in a thicker oceanic crust and basaltic seafloor, while non-volcanic segments receive little to no melt; therefore, accretion is mainly tectonic, resulting in a thinner oceanic crust and mantle rocks exposed on the seafloor (Ding et al., 2022; Jokat et al., 2003; Michael et al., 2003; Niu et al., 2015). At the Mid Atlantic Ridge (MAR) and the Southwest Indian Ridge (SWIR), accretion in non-volcanic segments is dominated by detachment faults, leading to the exhumation of mantle rocks at the seafloor (Cannat et al., 2006; Escartín, Smith, et al., 2008; Sauter et al., 2013). At transform faults between ridge segments both spreading

Writing – original draft: Matthias Pilot, Vera Schlindwein
Writing – review & editing: Marie Jakobsen Lien, Lars Ottemöller, Thibaut Barreyre

modes can occur across the axis, with accretion at the inside corner typically being tectonic and accretion at the outside corners being magmatic (Yu et al., 2013). Asymmetric spreading and a locally waning magma supply favor the formation of detachment faults with initially high-angle normal faults rolling over to lower angles at shallow depths (Behn & Ito, 2008; Buck et al., 2005; Escartín, Smith, et al., 2008; MacLeod et al., 2009). With ongoing faulting, the emerging detachment fault migrates toward the axial volcanic ridge (AVR), leading to the formation of oceanic core complexes (OCC) (Escartín et al., 2017; MacLeod et al., 2009; Reston & Ranero, 2012; Tucholke et al., 1998). More commonly than forming OCCs, detachment faults are terminated during their rotation to lower angles and a new detachment forms (Reston & Ranero, 2012).

In the last decades microseismicity recorded by ocean bottom seismometer (OBS) deployments improved the understanding of the lithospheric structure and magmato-tectonic processes at slow and ultraslow spreading ridges on scales reaching from ridge segments (>100 km) (Meier et al., 2021; Schlindwein & Schmid, 2016) to local detachment faults (<5 km) (J. Chen, Crawford, & Cannat, 2023; DeMartin et al., 2007; Parnell-Turner et al., 2020; Tao et al., 2020). Located earthquakes from OBS deployments at mature detachment faults delineate an initially steep, 65–75° dipping fault plane that rolls over to angles of 30–40° at shallow depths (DeMartin et al., 2007; Parnell-Turner et al., 2017; Tao et al., 2020; Yu et al., 2018). Characteristically, the deep part of a detachment faults slips continuously with low magnitude earthquakes while the shallow part shows more infrequent, large magnitude seismicity (Parnell-Turner et al., 2020). Furthermore, stress accumulates within the footwall of the detachment fault and is released episodically along antithetic normal faults due to solid block rotation (DeMartin et al., 2007; Sandiford et al., 2021) or antithetic reverse faults due to bending related compression (Parnell-Turner et al., 2017). Despite the advancements in understanding of detachment fault processes by OBS deployments, studies are often time-limited between a few days and weeks. Especially with the episodic characteristics, long-term observations are needed for a better understanding.

Regardless of the relatively low magma supply at slow and ultraslow spreading ridges, hydrothermal activity is more abundant than expected (Baker et al., 2004; Edmonds et al., 2003; German et al., 1998). Active hydrothermal vent fields have been linked to areas with asymmetric accretion and thus detachment faults (Escartín, Smith, et al., 2008; Son et al., 2014). Depending on the magma-tectonic setting (Früh-Green et al., 2022), hydrothermal vent fields can be located above the hanging wall (DeMartin et al., 2007) or off axis on top of the exposed fault surface of an OCC (J. Chen, Crawford, & Cannat, 2023; Parnell-Turner et al., 2017). However, the interplay between tectonic processes and hydrothermal systems at slow and ultraslow spreading ridges has not been extensively studied.

To investigate the interplay between a detachment fault, the AVR, and a hydrothermal vent, we deployed a network of eight OBS around the Loki's Castle hydrothermal vent field (LCVF) for a time period of ∼11 months. LCVF is located on top of the AVR at the Mohns-Knipovich Ridge (MKR) intersection in the Norwegian-Greenland Sea where the Arctic Mid-Ocean Ridge forms an 80° northwards bend (Pedersen et al., 2010) (Figure 1). Spreading at the MKR intersection is asymmetric across the AVR and slow to ultraslow, with a full spreading rate of ∼13 mm/yr (Kreemer et al., 2014). On the western flank of the rift valley mantle rocks are exposed at the Schulz Massif (Bjerga et al., 2022), while the eastern flank is mainly covered by sediments from the Bear Island fan (Bruvoll et al., 2009) (Figure 1). Additionally, the western flank shows increased earthquake activity (Pirli et al., 2018) and tectonic uplift compared with the eastern flank (Bruvoll et al., 2009). The combination of asymmetry in spreading rate and apparent accretion mode are first indicators of possible detachment faulting in the area. Fluid circulation at LCVF is proposed to be driven by an underlying asymmetric magma chamber revealed from electromagnetic surveys (Johansen et al., 2019). Geochemical analysis of the high temperature black smoker fluids at LCVF shows a strong sedimentary influence on a mainly basalt-hosted hydrothermal system (Baumberger et al., 2016; Pedersen et al., 2010). Previous OBS deployments were focused within few hundreds of meters around the LCVF (Loviknes et al., 2020). With the continuous ∼11 months microseismicity data set, we aim to characterize the increased seismic activity on the western flank of the MKR intersection on the scale of tens of kilometers and investigate how it is linked to the hydrothermal system related to LCVF.

2. Materials and Methods

2.1. Data Set

Eight four-channel OBS were deployed around the LCVF and an active fault zone (Johansen et al., 2019) at the Mohns-Knipovich Ridge bend. With a station spacing of 3–8 km, we continuously recorded seismicity for

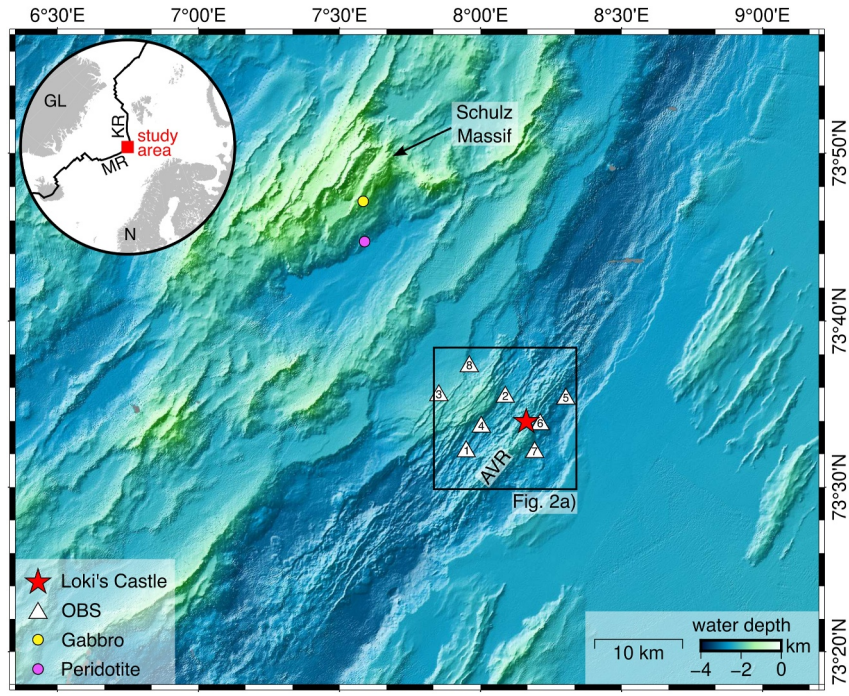

Figure 1. Bathymetry of the MKR intersection including an overview map showing its location in the Norwegian-Greenland Sea (top left). OBS network around LCVF and collected rock samples at the Schulz Massif (Bjerga et al., 2022). MR = Mohns Ridge, KR = Knipovich Ridge, GL = Greenland, N = Norway. Plate boundaries after Bird (2003), bathymetry data from Kartverket (www.kartverket.no).

~11 months between July 2019 and July 2020. The OBS were equipped with HighTech Inc hydrophones, Trillium Compact broadband seismometers, and K.U.M. 6D6 data loggers. Six OBS recorded with a sampling rate of 100 Hz, while LOK01 and LOK06 recorded with a sampling rate of 250 Hz (Figure 1). For processing, we resampled the data from LOK01 and LOK06 to 100 Hz. Their positions on the seafloor were determined by calculating two-thirds of the distance between the deployment and recovery positions, as the instruments rise twice as fast through the water column as they sink upon deployment. We estimate a maximum station uncertainty ~200 m. Resulting travel time inaccuracies are of the order of the pick uncertainty. The OBS clocks were synchronized during deployment and recovery. Using ambient noise cross-correlation (Hannemann et al., 2014) a non-linear clock drift was determined and subsequently corrected for.

2.2. Earthquake Detection and Phase Picking

To detect earthquakes from the continuous data set, migration-based Lassie detection software (Heimann et al., 2017) was used. By stacking characteristic functions for each station of the network, Lassie calculates an image function for each possible source location of an event within a given search grid. A detection is triggered, when a user defined threshold is exceeded. The performance of Lassie was evaluated by comparing its detections to manually detected events for 11 reference days, which were evenly distributed throughout the ~11 months deployment. We found that a detection threshold of 36 resulted in Lassie detecting small events while discarding background noise (Pilot & Schlindwein, 2024).

For phase picking of the Lassie-detected events, we used the deep-learning-based PhaseNet algorithm (Zhu & Beroza, 2019) with the model trained on the Northern California Earthquake catalog (model 190703–214543). A detection threshold of 0.3 was used for P- and S-phase detection. Following the approach by Pilot and Schlindwein (2024), we preliminarily located the picked events with HYPOCENTER (Lienert et al., 1986) as implemented in SEISAN (Havskov & Ottemöller, 1999; Havskov et al., 2020) and chose two subsets of events for which we subsequently revised phase picks manually: First, a subset of 1,534 best-constrained events within the network (root mean square residual (RMS) ≤ 0.2 s, picks at ≥seven stations, gap ≤ 120°) and second, a subset of 5,185 worst-constrained events. For the latter, we first revised events with an RMS > 0.5 s and, after another

location run, omitted events with an RMS > 0.5 s. From the remaining worst-constrained events, we revised another set of events with RMS > 0.4 s and individual pick residuals >|0.75| s.

2.3. Velocity Model and Station Correction Terms

With no relevant velocity model available for the area, we determined a 1D velocity model using PyVelest (Kissling et al., 1995). For this, we selected 386 events with a Lassie detection value ≥130 from the subset of 1,534 best-constrained and manually re-evaluated events (Section 2.2). For the inversion, we used three starting 1D models to randomly create 1,900 velocity models with varying layer thicknesses and velocities (Figure S1 in Supporting Information S1, Jeddi et al., 2021; Meier et al., 2021). Based on the 10 lowest RMS PyVelest models, we compiled two gradual 1D models for further analysis: A slower velocity model based on the two minimum RMS PyVelest models and a faster velocity model based on the other eight PyVelest models (Figure S1 in Supporting Information S1). To determine the Vp/Vs ratio and initial station corrections, we used HYPOCENTER and tested a range of Vp/Vs ratios while locating the subset of 386 events. For the slower velocity model, the minimum RMS solution was achieved with a Vp/Vs ratio of 1.81, while for the faster model, a Vp/Vs ratio of 2.04 gave the best results (Figure S2 in Supporting Information S1). To determine the final station corrections, we located the subset of 386 events once with NonLinLoc (Lomax et al., 2000, 2009) using the resulting hypocenter station correction terms as a priori station corrections with their corresponding velocity models and Vp/Vs ratios. Final station corrections were obtained as the average station residuals of the NonLinLoc solution (Table S1 in Supporting Information S1).

2.4. Earthquake Location

For the final event location, we used NonLinLoc with the Oct-Tree sampling algorithm (Lomax & Curtis, 2001). Since not all automatic picks were manually revised and the data set may still include erroneous phase picks, we applied the EDT_OT_WT inversion scheme, which downweighs outliers and can thus increase the location quality provided there is a sufficient number of picks available per event (Pilot & Schlindwein, 2024). To reliably identify outliers, we therefore required a minimum of 7 P-phase picks, resulting in 6,977 events to be located. We used a velocity grid of 551 × 551 × 421 (x, y, z) nodes with a spacing of 0.1 km in each direction and a search grid of 221 × 221 × 161 (x, y, z) nodes with a spacing of 0.25 km in each direction. We located the catalog with both previously described combinations of velocity models, Vp/Vs ratios, and station corrections.

To select well-located events for the subsequent interpretation, we used as quality control criteria the RMS (≤0.1 s), the average length of the three error-ellipsoid axes (≤1 km), and the hypocentral spread (distance between expectation and maximum-likelihood hypocenter, ≤0.3 km) (Figure S3 in Supporting Information S1). For the faster velocity model, this resulted in 3,975 well-located events as opposed to 3,909 for the slower velocity model. We decided to use in the following the results of the fast velocity model, as the seismic velocities appear closer to what can be expected regarding the geological context of a volcanically active area of a slow-spreading ridge. The main difference is the absolute depth (Figure S4 in Supporting Information S1) with the slower velocity model suggesting about 1 km deeper hypocenters. Although this is within the range of depth uncertainties, interpretations of absolute depths should therefore be done with care.

2.5. Magnitudes

Using SEISAN's Automag routine, we automatically determined event amplitudes within a 5 s window around picked S phases on Wood-Anderson simulated data from both horizontal components. If the signal-to-noise ratio was at least 1.5, the amplitudes were kept and the local magnitude (M_l) was calculated according to the equation by Hutton and Boore (1987) using the hypocentral distance based on the NonLinLoc maximum likelihood hypocenter location as distance:

$$M_l = \log_{10}(\text{amplitude [nm]}) + 1.11 \times \log_{10}(\text{distance [km]}) + 0.00189 \times \text{distance [km]} - 2.09 \quad (1)$$

2.6. Fault Plane Solutions

To determine focal mechanisms, we manually examined a subset of 162 events with magnitude $M_l \geq 2.5$ and P-phase picks at eight stations. P-phase polarities were picked on unfiltered waveforms and we kept 85 events with polarity readings at all eight stations. Fault plane solutions were iteratively searched both with SKHASH

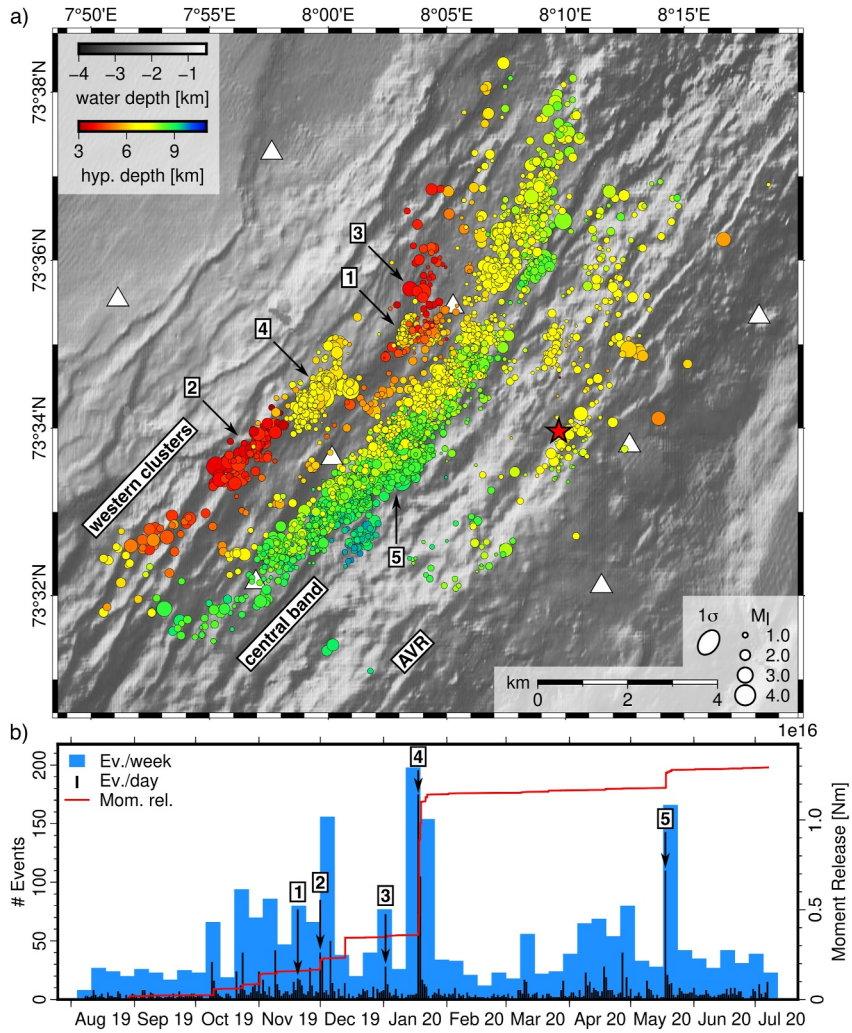

Figure 2. (a) Epicenters of the 3,975 well-located earthquakes scaled according to the local magnitude M_l. Colors refer to hypocentral depth below sea level. Red star = Loki's Castle hydrothermal vent field, white triangles = OBS stations. Three groups of seismicity are indicated by names and five clusters of events by numbers 1–5. Average location uncertainty is indicated by the 1σ error-ellipse. Bathymetry from the Center for Deep Sea Research (UiB) and Norwegian Petroleum Directorate (NPD, now Norwegian Offshore Directorate) (https://kartkatalog.geonorge.no/metadata/dyphavsundersoekelser-data/723af09b-cc8d-40eb-91a0-3a97093b83c9; Survey name: GS08; NPD survey name: 2008-UiB-01; 2008). (b) Weekly (blue bars) and daily (black bars) seismicity rate above Mc = 1.0 and moment release (red line) of the 3,975 well-located events during the deployment period. The numbers refer to the clusters shown in (a).

(Hardebeck, 2002; Skoumal et al., 2024) and FOCMEC as implemented in SEISAN (Havskov et al., 2020; Snoke, 2003). We used station azimuths and takeoff angles given by the NonLinLoc hypocenter solutions. We did not allow for any polarity errors and kept only solutions where SKHASH and FOCMEC agreed, resulting in 30 solutions. Polarity picks of these solutions were critically revised and we only kept events with indisputably clear P-phase polarity readings (Figure S5 in Supporting Information S1), leaving a total of 13 SKHASH solutions (Figure 5a, Table S2 in Supporting Information S1).

3. Results

Our catalog of 3,975 well-located events shows local magnitudes ranging from 0.2 to 4.4 (Figure 2a, Figure S3 in Supporting Information S1). The average seismicity rate above a magnitude of completeness of Mc = 1.0 is 7.5 events per day. The general seismicity rate based on the 6,977 locatable events is 20.8 events per day. The location results show that most of the recorded seismicity occurred west of the AVR with no significant seismicity east of the

AVR (Figure 2a). We distinguish three groups of seismicity with different characteristics, which will be described in the following: a central band of seismicity, western clusters of seismicity, and the AVR seismicity (Figure 2a).

3.1. Central Band of Seismicity

The majority of the earthquakes are located in a central band of seismicity northwest of the AVR. The band shows a sharp boundary toward the AVR and follows its strike in a SSW-NNE direction (Figure 2a). Seismicity within this band is located at depths of 5–10 km below sea level (Figure 3d) and occurs mainly continuously in time throughout the deployment period. An episode of increased seismicity with the second highest daily event rate is also located within the central band of seismicity (Figures 2 and 4, cluster 5). Toward the northeast, the seismicity of this band shallows by ∼1 km (Figure 3d) and its strike changes to a more SW-NE direction. A ∼1 km wide gap in seismicity can be seen at the location of the change in strike direction (Figure 2a). The band of seismicity dips southeastwards with dip angles increasing from ∼55° at the outside edges (Figures 3b and 3g) to ∼75° in the central part (Figure 3e). Fault plane solutions of this group of seismicity are either poorly constrained, southwest-northeast striking normal faulting mechanisms (Figure 5a, events 12, 13) or ambiguous between steeply southwest dipping and oblique normal faulting mechanisms (Figure 5a, events 1, 3, 8, 9, 10, 11).

3.2. Western Seismicity Clusters

The second group of earthquakes is located west of the central band and is clustered in both space and time (Figures 2 and 4, clusters 1–4). Earthquakes of this group are located at depths between 3 and 8 km, occur episodically throughout the deployment, and have comparably large magnitudes. Within these clusters, there are two types of seismicity. First, clusters 1 and 4 are located at depths between 6 and 8 km (Figure 2a). Hypocenters from both clusters indicate a steeply northwestward dipping plane (Figures 3c and 3e), partially in agreement with fault plane solutions from two events within cluster 4 (Figure 5b, events 4 and 6). Cluster 4 has the largest stepwise increase in moment release of the deployment (Figure 2b) with 351 events occurring within 36 hr, including four $M_l > 3.9$ events. Cluster 1 does not show a stepwise increase in moment release (Figure 2b). Second, clusters 2 and 3 are located at shallow depths between 3 and 5 km (Figures 2a, 3b, and 3g). Here, the seismicity clusters show either a hypocentral trend with a southeastward dip (Figure 3g) or no obvious hypocentral trend (Figure 3b). For cluster 2, the fault plane solution also shows a southeastward dip (Figure 5c, event 2). Compared to cluster 3, the increase in moment release is larger for cluster 2 (Figure 2b).

3.3. Axial Volcanic Ridge Seismicity

The third group of events is located along AVR with sparse, non-episodic seismicity at depths of 6–10 km (Figures 2a and 3f). Just northeast of LCVF, maximum earthquake depths are shallowing by up to ∼3 km along the AVR (Figure 3f) and below LCVF, the hypocenters are less scattered compared to the seismicity along the rest of the AVR (Figures 2a and 3c). Northwest of LCVF, a gap in seismicity can be seen (Figures 2a and 3c).

4. Discussion and Interpretation

4.1. Thermal Regime at the Mohns-Knipovich Ridge Intersection

Earthquakes are a result of brittle rock failure and thus the maximum depth of seismicity can be interpreted as indication for the brittle-ductile transition (BDT) (W.-P. Chen & Molnar, 1983; Wiens & Stein, 1983). The BDT is mainly temperature-controlled, corresponding to the ∼650°C isotherm (McKenzie et al., 2005; Schlindwein & Schmid, 2016), and its depth typically increases with decreasing spreading rates due to a limited amount of melt supply (J. Chen, Olive, & Cannat, 2023; Grevemeyer et al., 2019; Morgan & Chen, 1993). Compared to other seismicity studies from slow to ultraslow spreading ridges, the BDT at the MKR intersection is relatively shallow with 8–10 km depth (Figures 3d and 3f). At the Knipovich Ridge, for example, the BDT shallows toward the Logachev volcanic center to around 10 km (Meier et al., 2021) and along the SWIR microseismicity studies around hydrothermal vent fields have reported maximum depths of seismicity around 15 km (J. Chen, Crawford, & Cannat, 2023; Tao et al., 2020; Yu et al., 2018). Because of the orthogonal spreading at the MKR intersection (Bruvoll et al., 2009), the effective spreading rate is higher compared to the very oblique spreading Knipovich Ridge (Curewitz et al., 2010) or the slower spreading SWIR (Kreemer et al., 2014). Similar to the

10.1029/2024GC011732

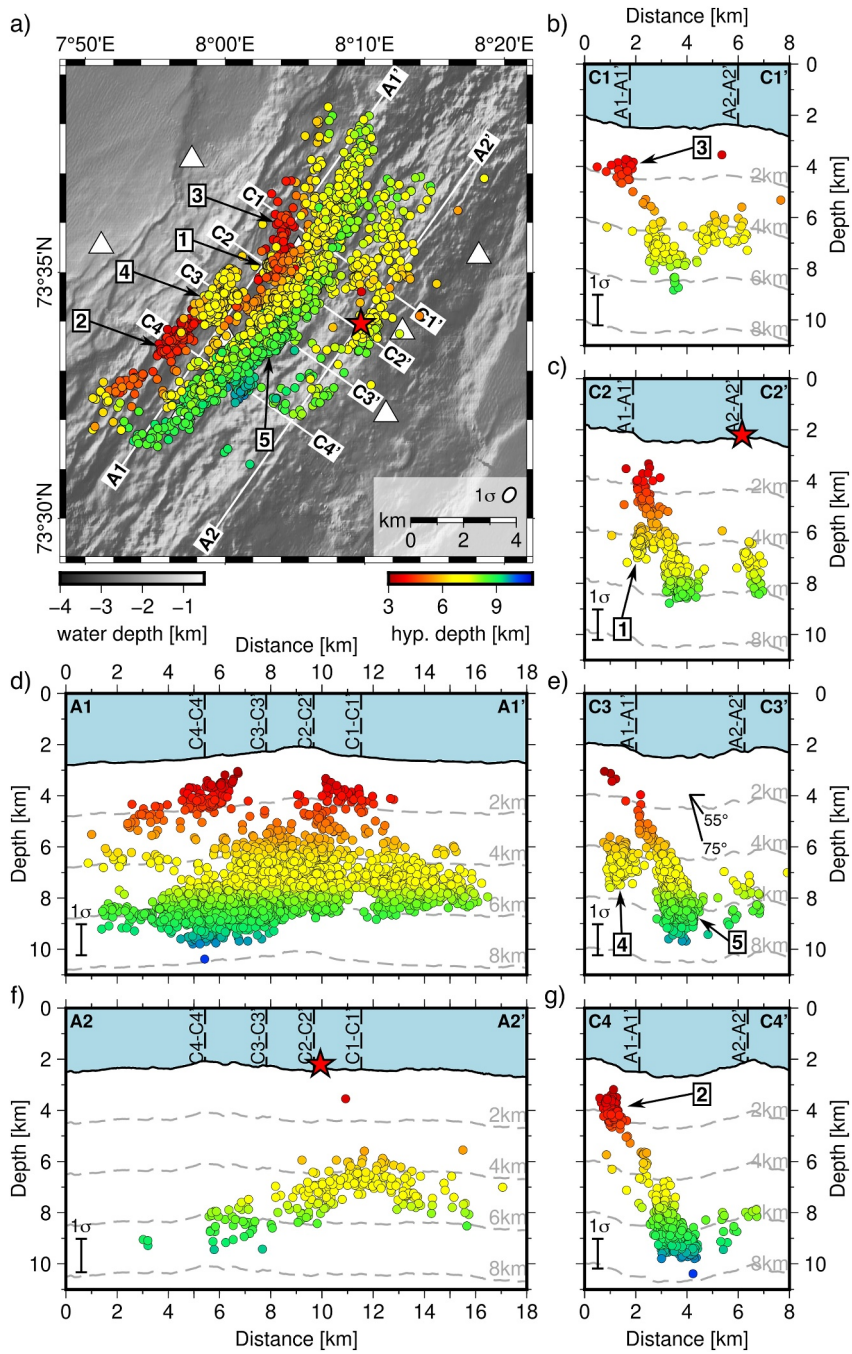

Figure 3. (a) Overview map showing the 3,975 well-located events and the locations of the cross-sections shown in (b)–(g). Red star indicates the position of Loki's Castle. Locations of clusters 1–5 are indicated by numbers. (b, c, e, g) Across-axis cross-sections C1–C1′, C2–C2′, C3–C3′, and C4–C4′ with projected earthquakes from ±0.7, ±0.7, ±1.3, ±1.1 km range, respectively. The average depth uncertainty as indicated by the 1σ error-bar. Locations of clusters 1–5 are indicated by numbers. (d, f) Along-axis cross-sections A1–A1′ and A2–A2′ with projected earthquakes from ±2.5 and ±1.5 km range, respectively. The average depth uncertainty as indicated by the 1σ error-bar.

results of this study, the BDT at hydrothermal vent sites along the MAR has been reported to be around 8 km (DeMartin et al., 2007; Grevemeyer & Reston, 2013; Horning et al., 2018).

We observe a local shallowing of the BDT by ~3 km along the AVR toward LCVF (Figure 3f). In addition, a gap in seismicity is located between the central band and the AVR seismicity, west of LCVF (Figures 2a and 3c).

10.1029/2024GC011732

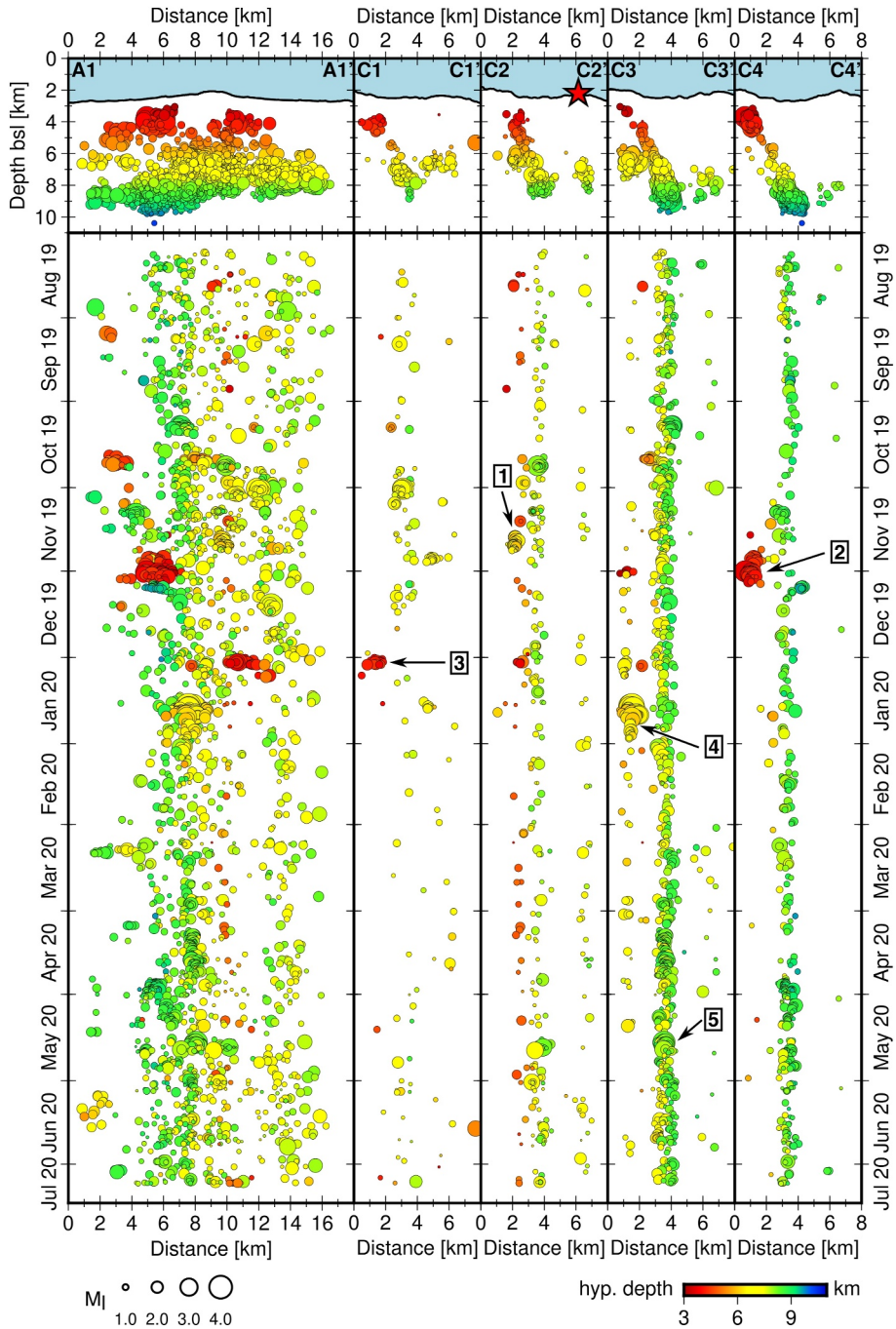

Figure 4. Cross-sections as shown in Figure 3 on top with the temporal evolution of seismicity below. Locations of clusters 1–5 are indicated by numbers. Red star indicates the projected position of Loki's Castle.

Inversion results from a controlled source electromagnetic profile across LCVF by Johansen et al. (2019) suggest an asymmetric mantle melt zone with the upper part being locally focused toward the west of the AVR. The location of this interpreted melt zone matches the described gap in seismicity west of LCVF. However, the observed deep seismicity of the central band (Figure 3c) is located in an area where Johansen et al. (2019) modeled isotherms above 1100°C, at which brittle behavior is not expected anymore.

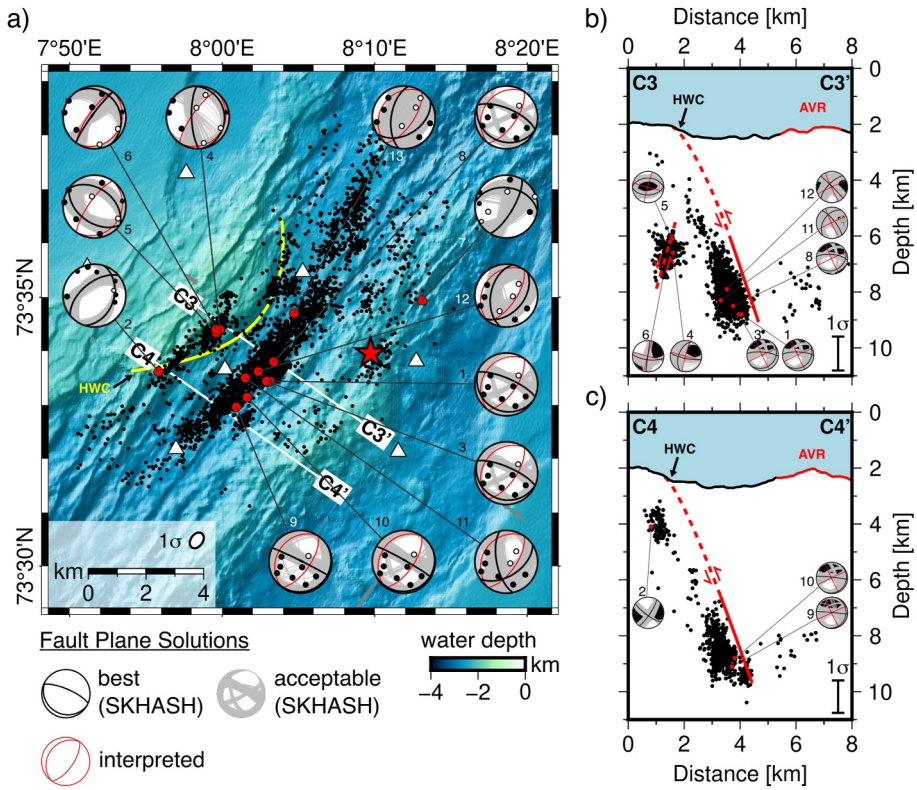

Figure 5. (a) All 13 SKHASH determined fault plane solutions (lower hemisphere projection). HWC = hanging-wall cutoff. P-phase polarities are shown as dots (black = compression, white = dilatation). Numbers refer to the event IDs (Table S1 in Supporting Information S1). Hypocenters of the 3,975 well-constrained events are shown in black, stations are indicated by white triangles, Loki's Castle is indicated by a red star. (b, c) Cross-sections similar to Figures 3e and 3g including fault plane solutions projected as half-spheres behind a vertical plane (quadrant colors from the best SKHASH solutions are plotted as background). Interpreted detachment fault shown by red line. AVR = axial volcanic ridge.

4.2. Early Stage Detachment Faulting

Most of the plate divergence at the MKR intersection is accommodated by an active fault structure on the western margin of the rift valley (Figure 3). Only sparse seismicity is observed along the AVR, and the eastern rift valley of the MKR intersection is not seismically active as the OBS network is sensitive for this area. Toward the Knipovich Ridge in the north, seismicity is more scattered across the rift valley (Figure 2a, Figure S6 in Supporting Information S1). This is typically observed along a symmetrically spreading ridge (Meier et al., 2021; Schlindwein & Schmid, 2016). Asymmetric spreading at slow-spreading ridges is a characteristic pre-requisite for the development of detachment faults on one side of the AVR (Escartín, Smith, et al., 2008). Dip angles from the deeper part of detachment faults at slow to ultraslow spreading ridges are reported to be around 65° (DeMartin et al., 2007; Parnell-Turner et al., 2017; Tao et al., 2020; Yu et al., 2018). A similar dip angle of 65–75° can be observed for the central part of the active fault structure at the MKR intersection (Figure 5b). For the deeper part of the fault we find two fault plane solutions with polarity readings roughly agreeing with a steeply dipping normal fault of ridge parallel strike as interpreted from the seismicity (Figure 5a, events 12 and 13). The ambiguity of the remaining six fault plane solutions for the deep part of the fault (Figure 5a, events 1, 3, 8, 9, 10, 11) can not be resolved given the OBS network geometry. However, the observed polarity readings of these events cannot be reconciled with the interpreted steeply dipping normal fault, suggesting additional tectonic complexity. A possible explanation for the few normal faulting solutions obtained could be that the deep part of the fault shows mainly continuous small magnitude seismicity, for which the determination of reliable polarity readings on all eight stations is difficult given the background noise in the marine environment.

The hanging wall of the fault does not show seismic activity, similar to observations from detachment faults at magmatic ridge segments (J. Chen, Crawford, & Cannat, 2023; DeMartin et al., 2007; Parnell-Turner et al., 2020).

The footwall of the fault is characterized by episodic, large magnitude earthquakes at shallow (3–5 km) and intermediate (6–8 km) depths (Figures 3b, 3c, 3e, 3g, and 4). Episodic shallow seismicity with large magnitudes in contrast to continuous deeper seismicity with small magnitudes has been proposed to be a characteristic feature of mature detachment faults (Parnell-Turner et al., 2020). Footwall seismicity has been observed during several deployments around active detachment faults at the MAR and SWIR (J. Chen, Crawford, & Cannat, 2023; DeMartin et al., 2007; Parnell-Turner et al., 2017).

The main difference between the results of this study and seismicity typically observed at mature detachment faults (Escartín et al., 2017; Smith et al., 2008) is that by connecting the continuously active deep part of the fault with the fault exposure observed in the bathymetry (Figures 5b and 5c), the fault does not show a fault roll-over to low angles. Instead, we see a steep-angle exposure of the fault and no corrugated surface in the bathymetry at the western rift margin of the MKR intersection (Figure 1). The young detachment fault at the Trans-Atlantic Geotraverse (TAG) hydrothermal vent site also shows no corrugated surface but a low-angle fault roll-over (DeMartin et al., 2007). With mantle rocks like gabbro and serpentinite being exposed at the Schulz massif toward the northwest of the study area, it seems likely that a detachment fault was previously active in the same area (Bjerga et al., 2022). Due to this and the described similarities in seismicity to mature detachment faults, we interpret the active fault structure west of the AVR at the MKR intersection to be an oceanic detachment fault at an early stage of the life cycle of OCCs (MacLeod et al., 2009).

4.3. Antithetic Footwall Faulting

We recorded episodic seismicity within the footwall of the detachment fault at depths of 6–8 km (Figure 4, cluster 1 and 4). Within both clusters, we observe no indicators of dike intrusions, for example, a clear propagation of events. Furthermore, there is no evidence for magma at shallow depths below the western flank (Bruvoll et al., 2009; Johansen et al., 2019). Without an active hydrothermal vent system at the western ridge flank and seismicity related to hydrothermal fluid circulation usually showing small magnitudes (Bohidar et al., 2024; Crawford et al., 2013), clusters 1 and 4 are most likely of tectonic origin. This is further strengthened by the fact that we see the largest jump in moment release during the deployment for cluster 4 (Figure 2b), indicating that stresses within the footwall accumulate over time and are released by large magnitude events. Seismological observations of similar footwall seismicity are rare, likely due to its episodic character (Parnell-Turner et al., 2020) and often short deployment times (e.g., J. Chen, Crawford, & Cannat, 2023). At the TAG detachment fault, focal mechanisms show antithetic 65° dipping normal faults at depths between 5 and 7 km (DeMartin et al., 2007). Events within the footwall of the 13°20′N detachment at depths between 4 and 8 km show a similar pattern to the seismicity at the TAG detachment fault and the results from this study, but were related to bending stresses being accumulated within the footwall, resulting in compression and antithetic reverse faulting (Parnell-Turner et al., 2017). Numerical models show that during detachment faulting, antithetic normal faults within the footwall initiate early during the formation of a detachment fault and remain active as it rolls over to lower angles with the antithetic normal faults moving away from the ridge valley (Bickert et al., 2020; Mezri et al., 2024; Sandiford et al., 2021).

The seismicity pattern of cluster 1 shows a hypocentral trend with an antithetic ∼75° dip (Figure 3b), but no reliable fault plane solutions for this cluster are available. For cluster 4, fault plane solutions for events 4 and 6 show a steeply dipping antithetic normal fault and polarity picks from event 6 allow for an interpreted 75° northwest dipping normal fault with a strike parallel to the spreading ridge (Figures 5a and 5b). However, the hypocentral trend is not as clear for cluster 4 (Figure 5b) as it is for cluster 1 (Figure 3c) and the fault plane solution and polarity picks for event 5 do not agree with an interpreted antithetic normal fault. Due to the limitations in the network geometry and size, we are not able to further constrain the mechanical behavior of the deeper footwall seismicity. With the origin most likely being tectonic and in partial agreement with results from numerical models and observed characteristics of footwall seismicity from other detachment faults, we interpret the seismicity of clusters 1 and 4 to be related to antithetic normal faulting.

4.4. Shallow Episodic and Deep Continuous Seismicity

A striking characteristic of the observed detachment fault seismicity at the MKR intersection is the contrast between continuous deep seismicity at 6–9 km depth and episodic shallow events at 3–5 km depth (Figure 4). At the TAG and 13° 20′ N OCCs, the deeper part of the detachment fault also shows continuous low-magnitude

seismicity (DeMartin et al., 2007; Parnell-Turner et al., 2017), likely being a characteristic observation for detachment faults (Parnell-Turner et al., 2020). However, at the MKR intersection we also observe episodes of increased seismicity within the deep part of the detachment fault (Figure 4), the most prominent being cluster 5 which occurred on 18 May 2020 and shows the second highest daily seismicity rate of the deployment with a clear stepwise increase in moment release (Figure 2b). This cluster occurred within the central region of the detachment fault where the dip is steepest (Figures 2a and 4), indicating that stress along the deeper part of the detachment fault is not exclusively released by continuous low-magnitude events but can also accumulate over time. Unfortunately, we could not constrain the focal mechanisms of events from cluster 5 in a reliable way.

The shallow seismicity within the footwall of the detachment fault at the MKR intersection ruptures mechanically differently compared to the deeper fault surface. Here, we observe short episodes of larger magnitude, normal faulting events (Figure 4, clusters 2 and 3, Figure 5c, event 2), or no seismicity at all (Figure 3d, shallow area below C2-C2′ and C3-C3′ intersections). At the mature 13° 20′N detachment fault, shallow large magnitude earthquakes have been interpreted to be an indicator of infrequent rupturing along the shallow part of the detachment fault (Parnell-Turner et al., 2020). Aseismic shallow parts of detachment faults have been observed at slow- and ultraslow spreading ridges (DeMartin et al., 2007; Parnell-Turner et al., 2017; Tao et al., 2020; Yu et al., 2018) and were linked to hydrothermal alteration of the fault zone, reducing the brittle strength of the rocks (Cannat et al., 2019; Escartín, Andreani, et al., 2008). The aseismic shallow area is located above the observed deeper episodic footwall seismicity (Figures 2a and 3c–3e, cluster 1 and 4). Potentially, here most of the stress was released within the deeper part of the footwall instead of the shallow part. Due to the episodic character of the shallow seismicity, we can also not exclude the possibility that the shallow part in this area was seismically active outside of the OBS deployment time.

4.5. Axial Volcanic Ridge Seismicity and the Hydrothermal System

Similar to observations at hydrothermal vent systems and inside corner detachment faults, only sparce seismicity occurs along the AVR (DeMartin et al., 2007; Parnell-Turner et al., 2020). Seismicity along the AVR at the MKR intersection is continuous in time (Figure 4) with no evidence during the 11 months recording period for episodic events such as magma intrusions that would appear as seismic swarms (Fischer et al., 2022; Meier et al., 2021). The only striking feature observed at the MKR intersection is that earthquakes are less scattered below the LCVF (Figures 2a and 3c). With no evidence for swarm activity, another possible interpretation could be thermal cracking as a result of hydrothermal cooling above a magma chamber. However, such events typically show smaller magnitudes than we observed (Bohidar et al., 2024; Crawford et al., 2013) and without reliable fault plane solutions, interpretation of this seismicity remains speculative.

The detachment fault at the MKR intersection initiates in the western rift valley (Figure 3c) and the magma chamber driving the high-temperature discharge at the LCVF (Johansen et al., 2019) is located eastwards of the fault surface. Typically, during ongoing detachment faulting, the locus of the spreading moves from the AVR to the detachment fault (MacLeod et al., 2009). At the TAG detachment fault, the magma chamber related to the hydrothermal vent field is located within the footwall of the detachment (M. Zhao et al., 2012). The TAG detachment fault is also at an early stage of the development; however, the locus of spreading appears to have moved toward the detachment fault. This aligns with the observation of the much less pronounced fault roll-over at shallow depth at the MKR intersection detachment (Figure 5b), which is therefore at an earlier stage than the TAG detachment. Increasing magmatic accretion apart from the detachment fault also terminates detachment faults, just as decreasing magmatic accreation is a prerequisite for the development of detachment faults (MacLeod et al., 2009; Y. Zhao et al., 2024).

With the Schulz massif in the northwest of the MKR intersection (Bjerga et al., 2022), there are indications for previous detachment faulting and its termination. Extended gaps in seismicity observed at the Logachev volcanic center (Meier et al., 2022) or the Segment 8 volcano (Schlindwein & Schmid, 2016) combined with earthquake swarms and increases in Vp/Vs ratios point to ongoing magmatic accretion processes. In comparison, the gap in seismicity observed at the MKR intersection is smaller and intrusion swarms are absent, suggesting that the MKR intersection currently does not experience strong magmatic activity. Within the ∼11 months recording time, there was no observable trend for the magmatic activity at the MKR intersection, which could indicate whether the emerging detachment fault will continue to develop or terminate.

5. Conclusions

The data set from the ∼11 months OBS deployment around LCVF shows that spreading is highly asymmetric at the MKR intersection with an emerging detachment fault on the western rift valley accommodating the majority of plate divergence. West of the AVR, we observe a gap in seismicity (Figure 2a) coinciding with a low resistivity area (Johansen et al., 2019), which we thus interpret as a melt zone. Along the AVR, the BDT shallows by about ∼3 km toward LCVF (Figure 3f), indicating a locally focused heat source.

The largest magnitude events of the deployment are located within the footwall of the detachment fault, where seismicity is strongly episodic and of tectonic origin (Figure 4). We interpret two clusters of events within the deeper footwall seismicity to be antithetic normal faulting (Figure 4 cluster 1 and 4, Figures 5a and 5b), agreeing with results from numerical models (Bickert et al., 2020; Mezri et al., 2024; Sandiford et al., 2021) and observations from more developed detachment faults (DeMartin et al., 2007). Footwall seismicity has so far only been reported at more developed detachment faults; at the MKR intersection, we observe that this already occurs during the earliest stages of detachment faulting.

Contrasting to the strongly episodic, large magnitude events within the footwall, the deeper part of the detachment fault is characterized by mainly continuous, small magnitude events. Fault plane solutions partially agree with a 65° southwest dipping normal fault observed from the hypocenters for the deep detachment fault seismicity (Figures 5a and 5b, events 12 and 13). However, the majority of the fault plane solutions indicate a more complex tectonic behavior for the detachment (Figure 5a).

Compared to the TAG detachment fault, which is also at an early stage, we do not observe a fault roll-over to low angles at shallow depths, typically observed at long-lived detachment faults, and the locus of spreading is located eastwards of the detachment fault. Thus, we interpret the MKR intersection detachment to be at an initial stage of detachment fault formation.

Data Availability Statement

The located earthquake catalog used in this study is available at Zenodo (Pilot et al., 2024). Raw, continuous seismic data are available at PANGEA (Barreyre et al., 2023a) and time-corrected miniseed data are available at GEOFON (Barreyre et al., 2023b). Figures 1–4, Figures S4 and S6 in Supporting Information S1 were created using PyGMT (Uieda et al., 2023), Figure 5, Figures S4 and S5 in Supporting Information S1 were created using Generic Mapping Tools, version 6 (Wessel et al., 2019). Seismic data were processed with ObsPy (Beyreuther et al., 2010) and SEISAN 12 (Havskov & Ottemöller, 1999; Havskov et al., 2020).

Acknowledgments
The authors thank the crew and scientists of the R/V G.O. Sars cruises for deployment and recovery of the OBS stations and the Centre of Deep Sea Research (CDeepSea) at the University of Bergen for funding and support. We thank editor Anne Paul and associate editor Vasiliki Mouslopoulou and gratefully acknowledge the reviews by Myrto Pirli and Rob Sohn, which substantially improved this manuscript. OBS were obtained from the German Instrument Pool for Amphibian Seismology DEPAS (Schmidt-Aursch & Haberland, 2017). Open access was funded by the AWI Open Access Publication Fund. Open Access funding enabled and organized by Projekt DEAL.

References

Baker, E. T., Edmonds, H. N., Michael, P. J., Bach, W., Dick, H. J. B., Snow, J. E., et al. (2004). Hydrothermal venting in magma deserts: The ultraslow-spreading Gakkel and Southwest Indian Ridges. *Geochemistry, Geophysics, Geosystems*, *5*(8), Q08002. https://doi.org/10.1029/2004GC000712

Barreyre, T., Ottemöller, L., Schlindwein, V., Pedersen, R. B., & Schmidt-Aursch, M. (2023a). Project LOKI: DEPAS ocean-bottom seismometer operations at Loki's Castle vent field in 2019-2020 [Dataset]. *PANGAEA*. https://doi.org/10.1594/PANGAEA.957222

Barreyre, T., Ottemöller, L., Schlindwein, V., Pedersen, R. B., & Schmidt-Aursch, M. (2023b). Project LOKI: DEPAS ocean-bottom seismometer operations at Loki's Castle vent field in 2019-2020 (p. ∼300G) [Dataset]. *GFZ Data Services*. https://doi.org/10.14470/3Z326135

Baumberger, T., Früh-Green, G. L., Thorseth, I. H., Lilley, M. D., Hamelin, C., Bernasconi, S. M., et al. (2016). Fluid composition of the sediment-influenced Loki's Castle vent field at the ultra-slow spreading Arctic Mid-Ocean Ridge. *Geochimica et Cosmochimica Acta*, *187*, 156–178. https://doi.org/10.1016/j.gca.2016.05.017

Behn, M. D., & Ito, G. (2008). Magmatic and tectonic extension at mid-ocean ridges: 1. Controls on fault characteristics. *Geochemistry, Geophysics, Geosystems*, *9*(8), Q08O10. https://doi.org/10.1029/2008GC001965

Beyreuther, M., Barsch, R., Krischer, L., Megies, T., Behr, Y., & Wassermann, J. (2010). ObsPy: A Python toolbox for seismology. *Seismological Research Letters*, *81*(3), 530–533. https://doi.org/10.1785/gssrl.81.3.530

Bickert, M., Lavier, L., & Cannat, M. (2020). How do detachment faults form at ultraslow mid-ocean ridges in a thick axial lithosphere? *Earth and Planetary Science Letters*, *533*, 116048. https://doi.org/10.1016/j.epsl.2019.116048

Bird, P. (2003). An updated digital model of plate boundaries. *Geochemistry, Geophysics, Geosystems*, *4*(3), 1027. https://doi.org/10.1029/2001GC000252

Bjerga, A., Stubseid, H. H., Pedersen, L. E. R., Beinlich, A., & Pedersen, R. B. (2022). A highly depleted and subduction-modified mantle beneath the slow-spreading Mohns Ridge. *Geochemistry, Geophysics, Geosystems*, *23*(11), e2022GC010585. https://doi.org/10.1029/2022GC010585

Bohidar, S., Crawford, W. C., & Cannat, M. (2024). Seismic constraints on hydrothermal circulation and magmato-tectonic interactions beneath Lucky Strike volcano, Mid-Atlantic Ridge. *Geochemistry, Geophysics, Geosystems*, *25*(4), e2024GC011441. https://doi.org/10.1029/2024GC011441

Bruvoll, V., Breivik, A. J., Mjelde, R., & Pedersen, R. B. (2009). Burial of the Mohn-Knipovich seafloor spreading ridge by the Bear Island Fan: Time constraints on tectonic evolution from seismic stratigraphy. *Tectonics*, *28*(4). https://doi.org/10.1029/2008TC002396

Buck, W. R., Lavier, L. L., & Poliakov, A. N. B. (2005). Modes of faulting at mid-ocean ridges. *Nature*, *434*(7034), 719–723. https://doi.org/10.1038/nature03358

Cannat, M., Sauter, D., Lavier, L., Bickert, M., Momoh, E., & Leroy, S. (2019). On spreading modes and magma supply at slow and ultraslow mid-ocean ridges. *Earth and Planetary Science Letters*, *519*, 223–233. https://doi.org/10.1016/j.epsl.2019.05.012

Cannat, M., Sauter, D., Mendel, V., Ruellan, E., Okino, K., Escartin, J., et al. (2006). Modes of seafloor generation at a melt-poor ultraslow-spreading ridge. *Geology*, *34*(7), 605–608. https://doi.org/10.1130/G22486.1

Chen, J., Crawford, W. C., & Cannat, M. (2023). Microseismicity and lithosphere thickness at a nearly-amagmatic oceanic detachment fault system. *Nature Communications*, *14*(1), 430. https://doi.org/10.1038/s41467-023-36169-w

Chen, J., Olive, J., & Cannat, M. (2023). Beyond spreading rate: Controls on the thermal regime of mid-ocean ridges. *Proceedings of the National Academy of Sciences of the United States of America*, *120*(45), e2306466120. https://doi.org/10.1073/pnas.2306466120

Chen, W.-P., & Molnar, P. (1983). Focal depths of intracontinental and intraplate earthquakes and their implications for the thermal and mechanical properties of the lithosphere. *Journal of Geophysical Research*, *88*(B5), 4183–4214. https://doi.org/10.1029/JB088iB05p04183

Crawford, W. C., Rai, A., Singh, S. C., Cannat, M., Escartin, J., Wang, H., et al. (2013). Hydrothermal seismicity beneath the summit of Lucky Strike volcano, Mid-Atlantic Ridge. *Earth and Planetary Science Letters*, *373*, 118–128. https://doi.org/10.1016/j.epsl.2013.04.028

Curewitz, D., Okino, K., Asada, M., Baranov, B., Gusev, E., & Tamaki, K. (2010). Structural analysis of fault populations along the oblique, ultraslow spreading Knipovich Ridge, North Atlantic Ocean, 74°30′N-77°50′N. *Journal of Structural Geology*, *32*(6), 727–740. https://doi.org/10.1016/j.jsg.2009.08.011

DeMartin, B. J., Sohn, R. A., Canales, J. P., & Humphris, S. E. (2007). Kinematics and geometry of active detachment faulting beneath the Trans-Atlantic Geotraverse (TAG) hydrothermal field on the Mid-Atlantic Ridge. *Geology*, *35*(8), 711. https://doi.org/10.1130/G23718A.1

Ding, W., Niu, X., Zhang, T., Chen, S., Liu, S., Tan, P., et al. (2022). Submarine wide-angle seismic experiments in the High Arctic: The JASMInE Expedition in the slowest spreading Gakkel Ridge. *Geosystems and Geoenvironment*, *1*(3), 100076. https://doi.org/10.1016/j.geogeo.2022.100076

Edmonds, H., Michael, P., Baker, E., Connelly, D., Snow, J., Langmuir, C., et al. (2003). Discovery of abundant hydrothermal venting on the ultraslow-spreading Gakkel Ridge in the Arctic Ocean. *Nature*, *421*(6920), 252–256. https://doi.org/10.1038/nature01351

Escartín, J., Andreani, M., Hirth, G., & Evans, B. (2008). Relationships between the microstructural evolution and the rheology of talc at elevated pressures and temperatures. *Earth and Planetary Science Letters*, *268*(3), 463–475. https://doi.org/10.1016/j.epsl.2008.02.004

Escartín, J., Mével, C., Petersen, S., Bonnemains, D., Cannat, M., Andreani, M., et al. (2017). Tectonic structure, evolution, and the nature of oceanic core complexes and their detachment fault zones (13°20′N and 13°30′N, Mid Atlantic Ridge). *Geochemistry, Geophysics, Geosystems*, *18*(4), 1451–1482. https://doi.org/10.1002/2016GC006775

Escartín, J., Smith, D. K., Cann, J., Schouten, H., Langmuir, C. H., & Escrig, S. (2008). Central role of detachment faults in accretion of slow-spreading oceanic lithosphere. *Nature*, *455*(7214), 790–794. https://doi.org/10.1038/nature07333

Fischer, T., Hrubcová, P., Salama, A., Doubravová, J., Ágústsdóttir, T., Gudnason, E. Á., et al. (2022). Swarm seismicity illuminates stress transfer prior to the 2021 Fagradalsfjall eruption in Iceland. *Earth and Planetary Science Letters*, *594*, 117685. https://doi.org/10.1016/j.epsl.2022.117685

Früh-Green, G. L., Kelley, D. S., Lilley, M. D., Cannat, M., Chavagnac, V., & Baross, J. A. (2022). Diversity of magmatism, hydrothermal processes and microbial interactions at mid-ocean ridges. *Nature Reviews Earth & Environment*, *3*(12), 852–871. https://doi.org/10.1038/s43017-022-00364-y

German, C. R., Baker, E. T., Mevel, C., & Tamaki, K., & the FUJI Science Team. (1998). Hydrothermal activity along the southwest Indian Ridge. *Nature*, *395*(6701), 490–493. https://doi.org/10.1038/26730

Grevemeyer, I., Hayman, N. W., Lange, D., Peirce, C., Papenberg, C., Van Avendonk, H. J. A., et al. (2019). Constraining the maximum depth of brittle deformation at slow- and ultraslow-spreading ridges using microseismicity. *Geology*, *47*(11), 1069–1073. https://doi.org/10.1130/G46577.1

Grevemeyer, I., & Reston, T. J. (2013). Microseismicity of the Mid-Atlantic Ridge at 7°S–8°15′S and at the Logatchev Massif oceanic core complex at 14°40′N-14°50′N. *Geochemistry, Geophysics, Geosystems*, *14*(9), 3532–3554. https://doi.org/10.1002/ggge.20197

Hannemann, K., Krüger, F., & Dahm, T. (2014). Measuring of clock drift rates and static time offsets of ocean bottom stations by means of ambient noise. *Geophysical Journal International*, *196*(2), 1034–1042. https://doi.org/10.1093/gji/ggt434

Hardebeck, J. L. (2002). A new method for determining first-motion focal mechanisms. *Bulletin of the Seismological Society of America*, *92*(6), 2264–2276. https://doi.org/10.1785/0120010200

Havskov, J., & Ottemöller, L. (1999). SeisAn earthquake analysis software. *Seismological Research Letters*, *70*(5), 532–534. https://doi.org/10.1785/gssrl.70.5.532

Havskov, J., Voss, P. H., & Ottemöller, L. (2020). Seismological observatory software: 30 yr of SEISAN. *Seismological Research Letters*, *91*(3), 1846–1852. https://doi.org/10.1785/0220190313

Heimann, S., Kriegerowski, M., Isken, M., Cesca, S., Daout, S., Grigoli, F., et al. (2017). Pyrocko—An open-source seismology toolbox and library. *GFZ Data Services*. https://doi.org/10.5880/GFZ.2.1.2017.001

Horning, G., Sohn, R. A., Canales, J. P., & Dunn, R. A. (2018). Local seismicity of the rainbow massif on the Mid-Atlantic Ridge. *Journal of Geophysical Research: Solid Earth*, *123*(2), 1615–1630. https://doi.org/10.1002/2017JB015288

Hutton, L. K., & Boore, D. M. (1987). The ML scale in southern California. *Bulletin of the Seismological Society of America*, *77*(6), 2074–2094. https://doi.org/10.1785/BSSA0770062074

Jeddi, Z., Ottemöller, L., Sørensen, M. B., Rezaei, S., Gibbons, S. J., Strømme, M. L., et al. (2021). Improved seismic monitoring with OBS deployment in the Arctic: A pilot study from offshore western Svalbard. *Seismological Research Letters*, *92*(5), 2705–2717. https://doi.org/10.1785/0220200471

Johansen, S. E., Panzner, M., Mittet, R., Amundsen, H. E. F., Lim, A., Vik, E., et al. (2019). Deep electrical imaging of the ultraslow-spreading Mohns Ridge. *Nature*, *567*(7748), 379–383. https://doi.org/10.1038/s41586-019-1010-0

Jokat, W., Ritzmann, O., Schmidt-Aursch, M. C., Drachev, S., Gauger, S., & Snow, J. (2003). Geophysical evidence for reduced melt production on the Arctic ultraslow Gakkel mid-ocean ridge. *Nature*, *423*(6943), 962–965. https://doi.org/10.1038/nature01706

Kissling, E., Kradolfer, U., & Maurer, H. (1995). Velest user's guide—Short introduction. *Institute of Geophysics, ETH Zurich*, *1*.

Kreemer, C., Blewitt, G., & Klein, E. C. (2014). A geodetic plate motion and global strain rate model. *Geochemistry, Geophysics, Geosystems*, *15*(10), 3849–3889. https://doi.org/10.1002/2014GC005407

Lienert, B. R., Berg, E., & Frazer, L. N. (1986). HYPOCENTER: An earthquake location method using centered, scaled, and adaptively damped least squares. *Bulletin of the Seismological Society of America*, *76*(3), 771–783. https://doi.org/10.1785/BSSA0760030771

Lomax, A., & Curtis, A. (2001). Fast probabilistic earthquake location in 3D models using Oct-Tree importance sampling. *Geophysical Research Abstracts*, *3*. https://www.researchgate.net/publication/302951135

Lomax, A., Michelini, A., & Curtis, A. (2009). Earthquake location, direct, global-search methods. In R. A. Meyers (Ed.), *Encyclopedia of complexity and systems science* (pp. 1–33). Springer. https://doi.org/10.1007/978-3-642-27737-5_150-2

Lomax, A., Virieux, J., Volant, P., & Berge-Thierry, C. (2000). Probabilistic earthquake location in 3D and layered models. In C. H. Thurber, & N. Rabinowitz (Eds.), *Advances in seismic event location* (pp. 101–134). Springer. https://doi.org/10.1007/978-94-015-9536-0_5

Loviknes, K., Jeddi, Z., Ottemöller, L., & Barreyre, T. (2020). When clocks are not working: OBS time correction. *Seismological Research Letters*, *91*(4), 2247–2258. https://doi.org/10.1785/0220190342

MacLeod, C. J., Searle, R. C., Murton, B. J., Casey, J. F., Mallows, C., Unsworth, S. C., et al. (2009). Life cycle of oceanic core complexes. *Earth and Planetary Science Letters*, *287*(3), 333–344. https://doi.org/10.1016/j.epsl.2009.08.016

Magde, L. S., & Sparks, D. W. (1997). Three-dimensional mantle upwelling, melt generation, and melt migration beneath segment slow spreading ridges. *Journal of Geophysical Research*, *102*(B9), 20571–20583. https://doi.org/10.1029/97JB01278

McKenzie, D., Jackson, J., & Priestley, K. (2005). Thermal structure of oceanic and continental lithosphere. *Earth and Planetary Science Letters*, *233*(3–4), 337–349. https://doi.org/10.1016/j.epsl.2005.02.005

Meier, M., Schlindwein, V., & Schmid, F. (2022). Magmatic activity and dynamics of melt supply of volcanic centers of ultraslow spreading ridges: Hints from local earthquake tomography at the Knipovich Ridge. *Geochemistry, Geophysics, Geosystems*, *23*(10), e2021GC010210. https://doi.org/10.1029/2021gc010210

Meier, M., Schlindwein, V., Scholz, J.-R., Geils, J., Schmidt-Aursch, M. C., Krüger, F., et al. (2021). Segment-scale seismicity of the ultraslow spreading Knipovich Ridge. *Geochemistry, Geophysics, Geosystems*, *22*(2), e2020GC009375. https://doi.org/10.1029/2020gc009375

Mezri, L., García-Pintado, J., Pérez-Gussinyé, M., Liu, Z., Bach, W., & Cannat, M. (2024). Tectonic controls on melt production and crustal architecture during magma-poor seafloor spreading. *Earth and Planetary Science Letters*, *628*, 118569. https://doi.org/10.1016/j.epsl.2024.118569

Michael, P. J., Langmuir, C. H., Dick, H. J. B., Snow, J. E., Goldstein, S. L., Graham, D. W., et al. (2003). Magmatic and amagmatic seafloor generation at the ultraslow-spreading Gakkel Ridge, Arctic Ocean. *Nature*, *423*(6943), 956–961. https://doi.org/10.1038/nature01704

Morgan, J. P., & Chen, Y. J. (1993). The genesis of oceanic crust: Magma injection, hydrothermal circulation, and crustal flow. *Journal of Geophysical Research*, *98*(B4), 6283–6297. https://doi.org/10.1029/92JB02650

Niu, X., Ruan, A., Li, J., Minshull, T. A., Sauter, D., Wu, Z., et al. (2015). Along-axis variation in crustal thickness at the ultraslow spreading Southwest Indian Ridge (50°E) from a wide-angle seismic experiment. *Geochemistry, Geophysics, Geosystems*, *16*(2), 468–485. https://doi.org/10.1002/2014GC005645

Parnell-Turner, R., Sohn, R. A., Peirce, C., Reston, T. J., MacLeod, C. J., Searle, R. C., & Simão, N. M. (2017). Oceanic detachment faults generate compression in extension. *Geology*, *45*(10), 923–926. https://doi.org/10.1130/G39232.1

Parnell-Turner, R., Sohn, R. A., Peirce, C., Reston, T. J., MacLeod, C. J., Searle, R. C., & Simão, N. M. (2020). Seismicity trends and detachment fault structure at 13°N, Mid-Atlantic Ridge. *Geology*, *49*(3), 320–324. https://doi.org/10.1130/g48420.1

Pedersen, R. B., Rapp, H. T., Thorseth, I. H., Lilley, M. D., Barriga, F. J. A. S., Baumberger, T., et al. (2010). Discovery of a black smoker vent field and vent fauna at the Arctic Mid-Ocean Ridge. *Nature Communications*, *1*(1), 126. https://doi.org/10.1038/ncomms1124

Pilot, M., Jakobsen Lien, M., Ottemöller, L., & Schlindwein, V. (2024). Located earthquakes Loki's Castle 2019-2020 deployment [Dataset]. *Zenodo*. https://doi.org/10.5281/zenodo.12528350

Pilot, M., & Schlindwein, V. (2024). A practical approach to automatic earthquake catalog compilation in local OBS networks using deep-learning and network-based algorithms. *Seismological Research Letters*, *95*(4), 2124–2140. https://doi.org/10.1785/0220230182

Pirli, M., & Schweitzer, J., & the IPY Project Consortium. (2018). Seismicity along the Mohns—Knipovich Ridge bend and its correlation to ridge spreading rate. *Journal of Geodynamics*, *118*, 182–196. https://doi.org/10.1016/j.jog.2018.01.013

Reston, T. J., & Ranero, C. R. (2012). The 3-D geometry of detachment faulting at mid-ocean ridges. *Geochemistry, Geophysics, Geosystems*, *12*(7), 1–19. https://doi.org/10.1029/2011GC003666

Sandiford, D., Brune, S., Glerum, A., Naliboff, J., & Whittaker, J. M. (2021). Kinematics of footwall exhumation at oceanic detachment faults: Solid-block rotation and apparent unbending. *Geochemistry, Geophysics, Geosystems*, *22*(4), 1–12. https://doi.org/10.1029/2021GC009681

Sauter, D., Cannat, M., Rouméjon, S., Andreani, M., Birot, D., Bronner, A., et al. (2013). Continuous exhumation of mantle-derived rocks at the Southwest Indian Ridge for 11 million years. *Nature Geoscience*, *6*(4), 314–320. https://doi.org/10.1038/ngeo1771

Schlindwein, V., & Schmid, F. (2016). Mid-ocean-ridge seismicity reveals extreme types of ocean lithosphere. *Nature*, *535*(7611), 276–279. https://doi.org/10.1038/nature18277

Schmidt-Aursch, M. C., & Haberland, C. (2017). DEPAS (Deutscher Geräte-Pool für amphibische Seismologie): German instrument pool for amphibian seismology. *Journal of Large-Scale Research Facilities JLSRF*, *3*, A122. https://doi.org/10.17815/jlsrf-3-165

Skoumal, R. J., Hardebeck, J. L., & Shearer, P. M. (2024). SKHASH: A Python package for computing earthquake focal mechanisms. *Seismological Research Letters*, *95*(4), 2519–2526. https://doi.org/10.1785/0220230329

Smith, D. K., Escartín, J., Schouten, H., & Cann, J. R. (2008). Fault rotation and core complex formation: Significant processes in seafloor formation at slow-spreading mid-ocean ridges (Mid-Atlantic Ridge, 13°-15°N). *Geochemistry, Geophysics, Geosystems*, *9*(3), Q03003. https://doi.org/10.1029/2007GC001699

Snoke, J. A. (2003). 85.12 FOCMEC: FOCal MEChanism determinations. *International Geophysics*, *81*(PART B), 1629–1630. https://doi.org/10.1016/S0074-6142(03)80291-7

Son, J., Pak, S.-J., Kim, J., Baker, E. T., You, O.-R., Son, S.-K., & Moon, J.-W. (2014). Tectonic and magmatic control of hydrothermal activity along the slow-spreading Central Indian Ridge, 8°S–17°S. *Geochemistry, Geophysics, Geosystems*, *15*(5), 2011–2020. https://doi.org/10.1002/2013GC005206

Standish, J. J., Dick, H. J. B., Michael, P. J., Melson, W. G., & O'Hearn, T. (2008). MORB generation beneath the ultraslow spreading Southwest Indian Ridge (9–25°E): Major element chemistry and the importance of process versus source. *Geochemistry, Geophysics, Geosystems*, *9*(5), Q05004. https://doi.org/10.1029/2008GC001959

Tao, C., Seyfried, W. E., Lowell, R. P., Liu, Y., Liang, J., Guo, Z., et al. (2020). Deep high-temperature hydrothermal circulation in a detachment faulting system on the ultra-slow spreading ridge. *Nature Communications*, *11*(1), 1300. https://doi.org/10.1038/s41467-020-15062-w

Tucholke, B. E., Lin, J., & Kleinrock, M. C. (1998). Megamullions and mullion structure defining oceanic metamorphic core complexes on the Mid-Atlantic Ridge. *Journal of Geophysical Research*, *103*(B5), 9857–9866. https://doi.org/10.1029/98JB00167

Uieda, L., Tian, D., Leong, W. J., Schlitzer, W., Grund, M., Jones, M., et al. (2023). PyGMT: A Python interface for the generic mapping tools (version v0.9.0) [Computer software]. *Zenodo*. https://doi.org/10.5281/zenodo.7772533

Wessel, P., Luis, J. F., Uieda, L., Scharroo, R., Wobbe, F., Smith, W. H. F., & Tian, D. (2019). The generic mapping tools version 6. *Geochemistry, Geophysics, Geosystems*, *20*(11), 5556–5564. https://doi.org/10.1029/2019GC008515

Wiens, D. A., & Stein, S. (1983). Age dependence of oceanic intraplate seismicity and implications for lithospheric evolution. *Journal of Geophysical Research*, *88*(B8), 6455–6468. https://doi.org/10.1029/JB088iB08p06455

Yu, Z., Li, J., Liang, Y., Han, X., Zhang, J., & Zhu, L. (2013). Distribution of large-scale detachment faults on mid-ocean ridges in relation to spreading rates. *Acta Oceanologica Sinica*, *32*(12), 109–117. https://doi.org/10.1007/s13131-013-0397-y

Yu, Z., Li, J., Niu, X., Rawlinson, N., Ruan, A., Wang, W., et al. (2018). Lithospheric structure and tectonic processes constrained by micro-earthquake activity at the central ultraslow-spreading southwest Indian Ridge (49.2° to 50.8°E). *Journal of Geophysical Research: Solid Earth*, *123*(8), 6247–6262. https://doi.org/10.1029/2017JB015367

Zhao, M., Canales, J. P., & Sohn, R. A. (2012). Three-dimensional seismic structure of a Mid-Atlantic Ridge segment characterized by active detachment faulting (Trans-Atlantic Geotraverse, 25°55′N-26°20′N). *Geochemistry, Geophysics, Geosystems*, *13*(11), Q0AG13. https://doi.org/10.1029/2012GC004454

Zhao, Y., Ding, W., Manatschal, G., Wei, X., Ding, H., Tong, Z., & Zhao, J. (2024). Unraveling the link between magma and deformation during slow seafloor spreading. *Tectonophysics*, *889*, 230473. https://doi.org/10.1016/j.tecto.2024.230473

Zhu, W., & Beroza, G. C. (2019). PhaseNet: A deep-neural-network-based seismic arrival-time picking method. *Geophysical Journal International*, *216*(1), 261–273. https://doi.org/10.1093/gji/ggy423